AEROACOUSTIC ANALYSIS OF A HELICOPTER CONFIGURATION WITH DUCTED TAIL ROTOR

Jae Hun You*, **Nicolas Thouault***, **Christian Breitsamter*** and **Nikolas A. Adams***
***Institute of Aerodynamics and Fluid Mechanics, Technische Universität München**
Boltzmannstraße 15, D-85748 Garching, Germany
jaehun.you@aer.mw.tum.de

Keywords: *aeroacoustics, helicopter, ducted tail rotor, unsteady RANS, FW-H analogy*

Abstract

In the framework of the Bavarian research project FORLärm, numerical aeroacoustic investigations on a light weight transport helicopter with ducted tail rotor are carried out. To understand the noise generation mechanisms, a hybrid approach is applied for a forward flight condition. The flow field is calculated by an Unsteady Reynolds Averaged Navier-Stokes (URANS) method using Shear Stress Transport (SST) turbulence model. The helicopter Fenestron® configuration without main rotor has been modeled based on a structured mesh. A sliding mesh approach is employed to model the fan rotation. Based on instantaneous flow data provided by the URANS simulations, the computation of the acoustic far-field is performed by means of the Ffowcs Williams-Hawkings (FW-H) surface integral method. A complex flow topology is predicted by the URANS simulation. Flow separation occurs on the aft part of the fuselage thereby creating vortical structures convected downstream to the ducted tail rotor. A separation bubble caused by boundary layer separation at the fan inlet lip geometry is also observed. Based on results of the FW-H caculations, tonal noise components are identified. The sideband frequencies related to the blade passing frequency (BPF) obtained by the FW-H calculation match well with the analytical solution based on the phase modulation technique.

1 Introduction

Ducted tail rotor, also known as Fenestron®, is an innovative tail rotor concept of the conventional helicopter configuration (single main rotor and tail rotor configuration) to provide the necessary anti-torque thrust. Besides the significant improvement of operational safety near the ground and advancement of performance efficiency, the Fenestron® gives substantial acoustic benefits in contrast to the open tail rotor [1, 2]. For instance, the Fenestron® duct acts as an acoustic shield and the lower tip speed of the rotor blade also leads to decrease of acoustic power emission. Additionally, the rotor blades are unequally circumferentially distributed to spread the acoustic tonal energy over several frequencies thus reducing the noise annoyance at the blade passing frequency. For the reason outlined above, the Fenestron® has been recently successfully implemented on a variety of helicopters (e.g. EC 120, EC 135 and SA 365).

Numerous investigations related to aerodynamics [3, 4, 5] and aeroacoustics [6, 7] of the ducted tail rotor have been already conducted. However, accurate and detailed understanding of both aerodynamic and aeroacoustic phenomena, in particular, in forward flight condition still remain challenging considering the complex configuration and its flow field. Therefore, computational methods could help to unterstand the flow physics of the helicopter with ducted tail rotor and provide insights on the noise sources with

a view to improve the Fenestron$^{®}$ acoustic design. The aim of the present study is to document the flow physics linked to sound generation in the Fenestron$^{®}$ by means of a hybrid approach combining Unsteady Reynolds Averaged Navier-Stokes (URANS) Simulations and the Ffowcs Williams-Hawkings (FW-H) analogy.

Phase Modulation Technique. The idea of the phase modulation technique applied to the Fenestron$^{®}$ is to avoid acoustic repetition using circumferentially uneven spacing of rotor blades, thus the acoustic energy at the blade passing frequency is spread out over several frequencies. The even spacing of the Fenestron$^{®}$ blades has been redistributed by using the sinusoidal modulation described by [8]:

$$\theta_i' = \theta_i + \Delta\theta \sin(m\theta_i), \qquad (1)$$

where θ_i is the primary position of the ith blade, θ_i' is the rearranged position of ith blade after the modulation, $\Delta\theta$ is the modulation amplitude and m is the number of the repeated modulation in one revolution of the fan. The rearranged blade spacing of a 10-blade Fenestron$^{®}$ with $m = 2$ is presented in Fig. 1 (a).

By using the classical sinusoidal phase modulation equation, the pressure amplitude generating from a rotating fan with modulated spacing can be then predicted by [8]:

$$p(t) = A_0 \sin(2\pi F_0 t + \Delta\phi \sin 2\pi\nu t), \qquad (2)$$

with A_0 being the pressure amplitude by the blade passing frequency, F_0 the blade passing frequency (BPF) resulting from multiplication of the number of blades I and rotational frequency of the fan f_R, $\nu = m f_R$ the modulation frequency and $\Delta\phi = I\Delta\theta$ the phase-modulation amplitude. For a more realistic prediction of the pressure amplitude of a fan with small number of blades ($I < 20$), Ewald et al. [8] rearranged this formulation by introducing Fourier analysis and sinusoidal approximation of the pressure waveform produced by the fan:

$$p(t) = \hat{p}(t) + \sum_{n=1}^{\infty} B_n \sin(n\omega t) + \sum_{n=1}^{\infty} C_n \cos(n\omega t) \qquad (3)$$

where $\omega = 2\pi f_R$,

$$B_n = \frac{1}{2\pi} \sum_{i=1}^{I} \left\{ \frac{\sin[(D_i - n)\theta - D_i\theta_i]}{D_i - n} - \frac{\sin[(D_i + n)\theta - D_i\theta_i]}{D_i + n} \right\}_{\theta_i}^{\theta_{i+1}} \qquad (4)$$

and

$$C_n = -\frac{1}{2\pi} \sum_{i=1}^{I} \left\{ \frac{\cos[(D_i + n)\theta - D_i\theta_i]}{D_i + n} - \frac{\cos[(D_i - n)\theta - D_i\theta_i]}{D_i - n} \right\}_{\theta_i}^{\theta_{i+1}} \qquad (5)$$

with

$$D_i = \frac{2\pi}{(\theta_{i+1} - \theta_i)} \qquad (6)$$

The normalized pressure signal estimated by Eq. (3) is presented in Fig. 1, plotted as function of time (b) and of frequency (c), respectively. Parameters of the Fenestron$^{®}$ used for this calculation are listed in Table 1. It can be seen on Fig. 1 (c) that the phase modulation technique generates additional tones with significant amplitude near the 1st BPF distributing with the modulation frequency ν. The maximum amplitude occurs now below the 1st BPF.

Parameter	f_R	I	m	$\nu = m f_R$
Value	$59.73\,Hz$	10	2	$119.46\,Hz$

Table 1 Modulation parameters.

2 CFD Simulations

In this section, the numerical setup of the CFD simulation is described and the validation of CFD results using surface pressure distribution is given for a wind tunnel model with closed Fenestron$^{®}$. Furthermore, the detailed analysis of results is presented.
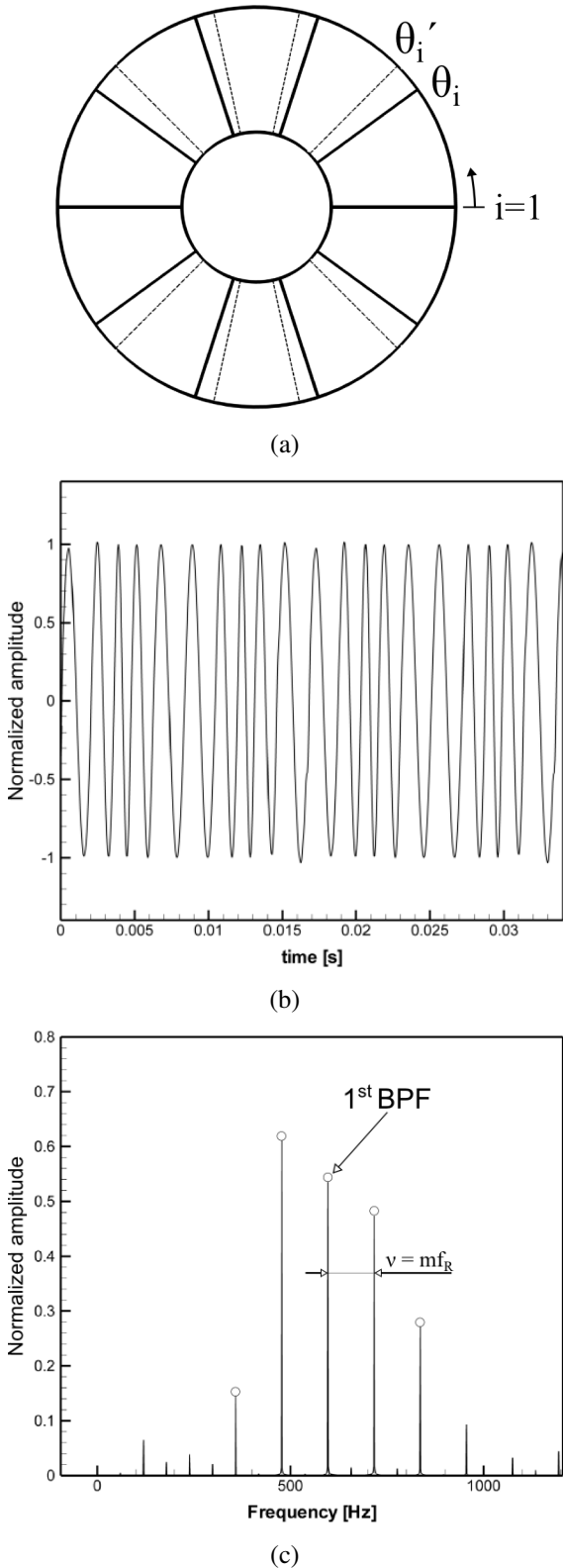
(a)

(b)

(c)

Fig. 1 Phase modulation of a 10-blade Fenestron®: (a) principle sketch of sinusoidal modulation, normalized pressure signal (b) in time domain and (c) in frequency domain, respectively.

2.1 CFD Numerical Setup

In this section, the investigated helicopter configuration is presented. An overview of the numerical setup and the computational approach used CFD is also given.

2.1.1 Geometry and Mesh Topology

The configuration investigated in the present study is a full-scale light transport helicopter with ducted tail rotor. The geometry includes detailed helicopter components consisting of fuselage, tailboom, empennage with vertical end plates and finally the complete Fenestron® (Fig. 2 (b)). The main rotor, the rotor head and landing skid are not included in the analysis. In addition, both engine intakes, as well as the exhausts are closed. The Fenestron® segment is divided into a rotor stage, a stator row, a shroud, an inlet and outlet lip, the vertical fin in the upper part and the bumper in the lower part. The rotor stage of the Fenestron® features 10 radially twisted rotor blades (Fig. 2 (a)). The fan geometry is precisely modeled including the blade tip clearance, as well as the cylindrical blade root connecting the blade to the rotor hub. The rotor blades are unevenly distributed in the circumferential direction by means of the sinusoidal modulation for the reduction of typical shrill noise of the Fenestron®. The stator stage consists of 10 rectangular-type vanes with a shaft fairing. Contrary to the rotor stage, the vanes could be considered as evenly spaced (counting the drive shaft fairing as an 11th stator vane). To take acoustic advantage, the stator blade is swept backward and leaned in the opposite of the fan rotational direction (counter-clockwise).

A structured grid is generated around this geometry by means of a multiblock meshing strategy with ANSYS ICEM CFD (Fig. 3). Due to the geometric complexity and the modeling of the rotating fan, the entire computational domain has been divided into three sub-domains labeled ROTOR, STATOR and DOMAIN (containing the remaining parts of the helicopter). The mesh in each sub-domain has been generated separately. Hence, the non-matching and overlap-
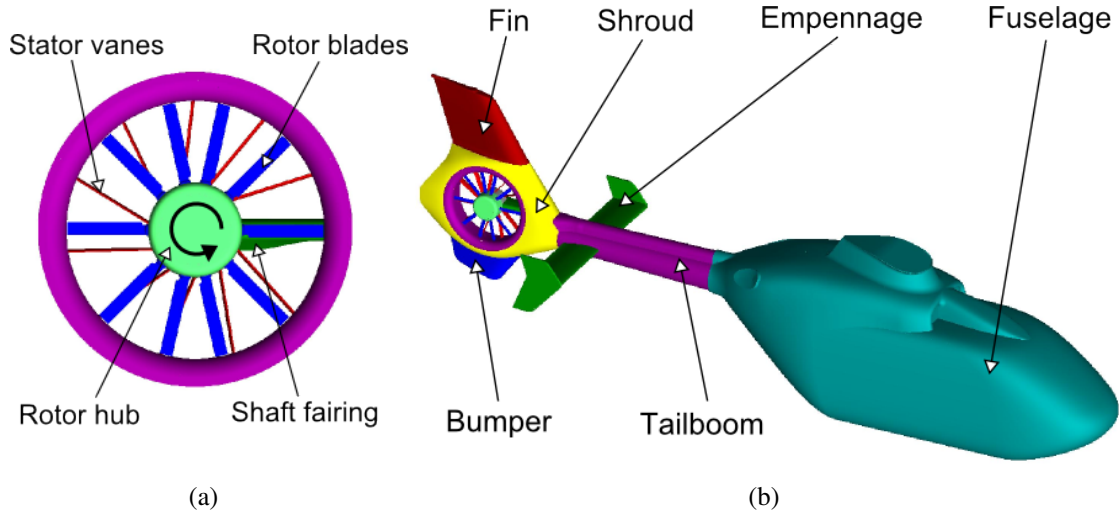
(a)   (b)

Fig. 2 Geometry of helicopter configuration with the Fenestron®.

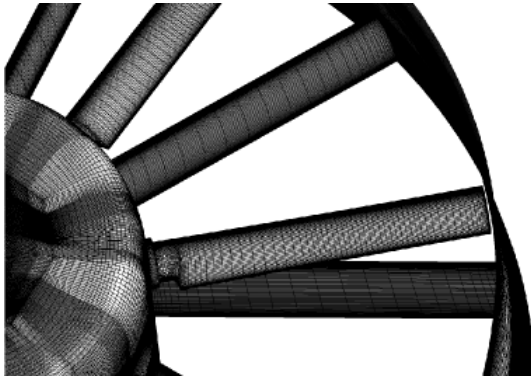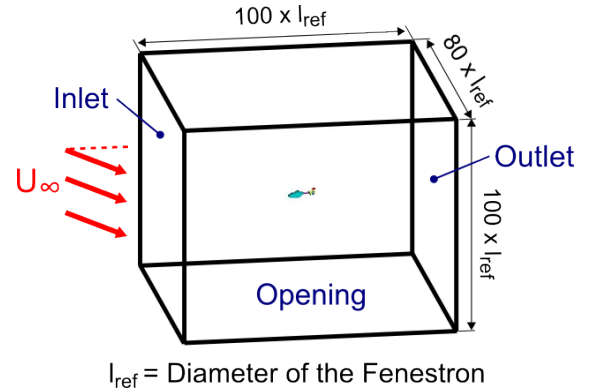**Fig. 3** Surface mesh on rotor blades and stator vanes.

Fig. 4 Sketch of the computational domain.

ping meshes caused by the connection between each part are treated by GGI (General Grid Interface) algorithm [9]. In order to predict flow separation accurately, the viscous sublayer is resolved using an O-grid topology. The height of the first cell layer has been set to achieve a value of $y^+ < 1$ (dimensionless wall distance).

Overall, 3400 blocks and 26.3×10^6 nodes are created around the geometry (11.8×10^6 in DO-MAIN, 10.6×10^6 in ROTOR and 3.9×10^6 nodes in STATOR, respectively).

2.1.2 Numerical Method of CFD

To calculate the unsteady viscous flow field, an URANS approach is employed. For this purpose, the commercial finite-volume-based Navier-Stokes solver ANSYS CFX (version 13.0) is used. The computational domain is a rectangular cuboid with the length of $100 \times l_{ref}$, the height of $100 \times l_{ref}$ and the width of $80 \times l_{ref}$ (Fig. 4). The angle of attack $\alpha = -2°$ and the sideslip angle $\beta = 0°$ are taken into account for the given forward flight condition (free stream velocity $U_\infty = 62.5\,m/s$, $Re_{1:1} = 4.1 \times 10^6$) by using an uniform velocity profile at the inlet with three explicit velocity components. An opening boundary condition [9] is used on the sidewalls, as well as on the top and bottom side of the computational domain with prescribed freestream velocity. The domain outlet is also defined by an opening boundary condition with a zero relative pressure averaged over the whole outlet surface to avoid an artificial pressure gradient down-

stream. For the spatial discretization, the high resolution scheme [9] is used. This method allows a dynamical adjustment of 1st order and 2nd order upwind scheme controlled by the blending factor $(0 \leq \beta \leq 1)$ to make a compromise between the accuracy and the robustness. For the unsteady calculation, an implicit second order backward Euler scheme is used for the temporal discretization. The $k - \omega$ Shear Stress Transport (SST) model by Menter [10] is adopted for the turbulence modeling. All the computations are performed fully turbulent. Since the blade tip Mach number given by the rotating speed is $M > 0.5$, the total energy model is employed to take into account of the compressibility effects in this region. The fan rotation is modeled by means of the sliding mesh technique, so that the ROTOR domain is connected to the stationary domain (DOMAIN and STATOR) by sliding interfaces (Fig. 5). A steady simulation using the Frozen Rotor approach has been conducted. The steady state result is used as initial solution for the unsteady simulation with Transient-Rotor-Stator method, which initializes an actual rotation of the fan grid. A constant time step $(\Delta t_{CFD} = 47\,\mu s)$ corresponding to $1°$ of fan rotation is taken for the unsteady calculations (360 time steps for a fan revolution).

All simulations have been conducted on the high performance computers (HLRB II / SuperMuc) of the Leibniz-Supercomputing center (LRZ) in Munich. A number of 40 to 120 processors per run has been used to compute 15 fan revolutions. The conv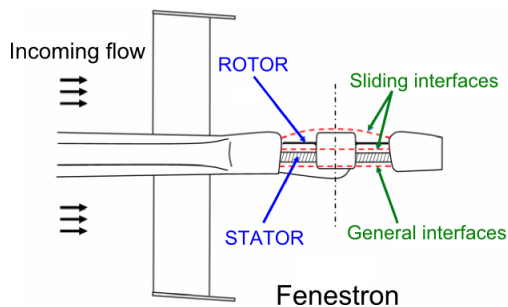ergence of the fan parameters is achieved after 5 fan revolutions. A strong variation of the axial force coefficient c_{axial} of rotor blades around a mean value can be observed for the next 10 revolutions (Fig. 6). Relevant flow data have been gathered on this time frame to feed the acoustic calculation.
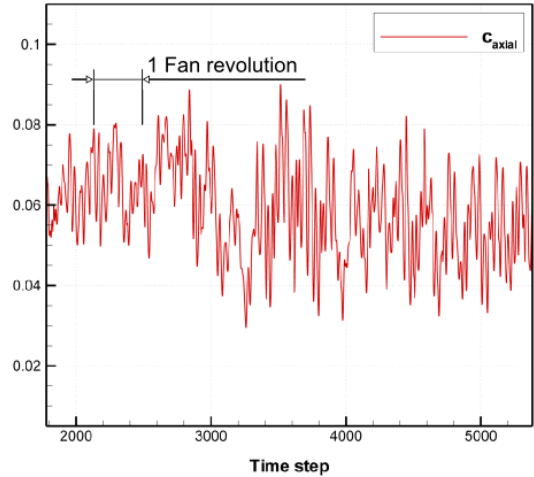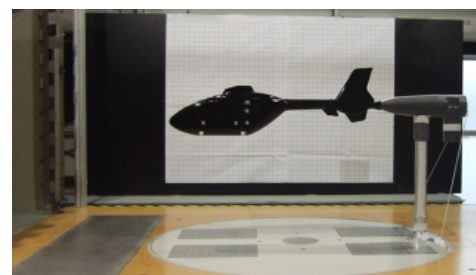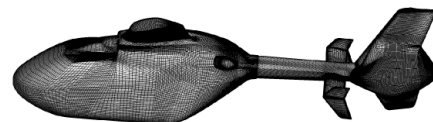

Fig. 6 Time history of the axial force coefficient c_{axial} of rotor blades for 10 fan revolutions.

2.2 Comparison to wind tunnel data

In order to evaluate the predictive capability of the numerical simulation, the results of the numerical simulation has been compared to wind tunnel data.
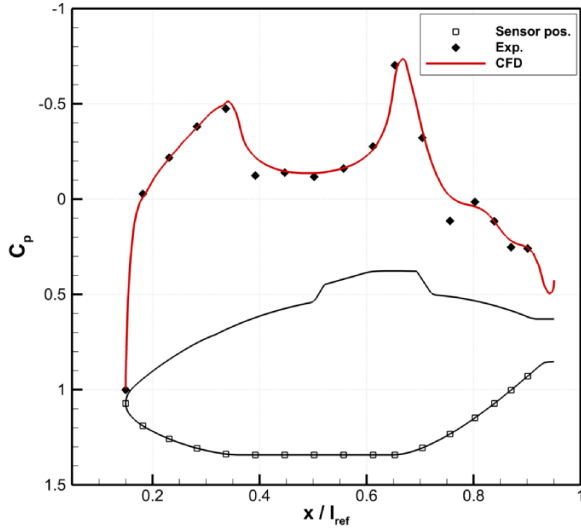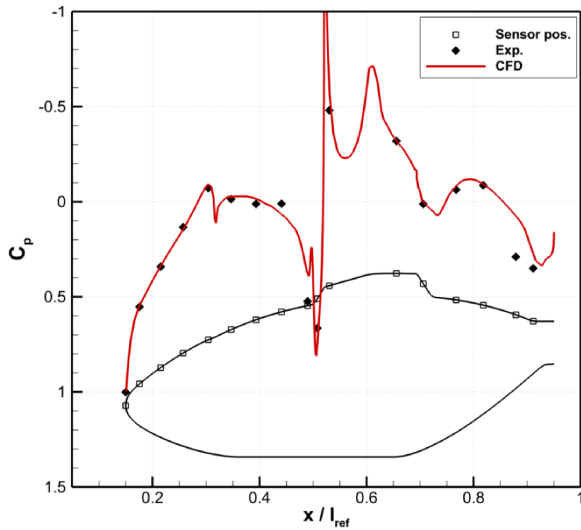

(a) wind tunnel model
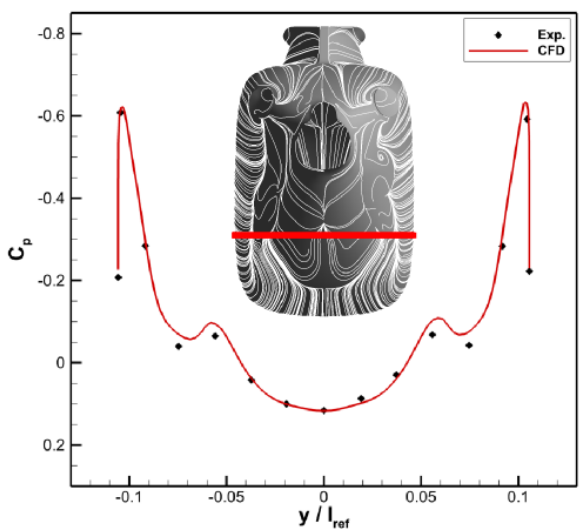

(b) numerical model

Fig. 7 Helicopter configuration with closed Fenestron$^{®}$.

Fig. 5 Schematic representation of the sliding mesh approach.

(a) lower side

(b) upper side

(c) horizontal plane

Fig. 8 Comparison of time averaged pressure coefficient distribution for $U_\infty = 40\,m/s$, $\alpha = -2°$ and $\beta = 0°$.
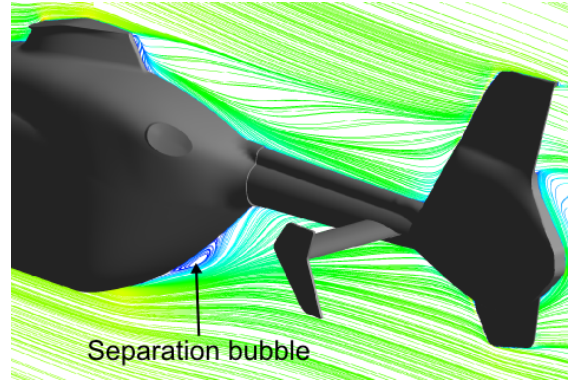

Separation bubble

Fig. 9 Separation bubble at the aft body of the fuselage visualized by time-averaged streamlines on the symmetry plane ($y/l_{ref} = 0$).

For this purpose, a numerical simulation of a scale down helicopter model (model size 1:7.333) with closed Fenestron$^{\circledR}$ is considered (Fig. 7 (b)). The experimental work has been conducted in the Göttingen-type wind tunnel A at the Institute of Aerodynamics and Fluid Mechanics of the Technische Universität München. This low speed wind tunnel has an open test section with dimensions of $1.8\,m \times 2.4\,m \times 4.8\,m$ (height, width and length, respectively). The free stream at the nozzle exit exhibits a homogeneous turbulence intensity of less than 0.4%. Both the numerical simulation with the closed Fenestron$^{\circledR}$ and the wind tunnel experiments were performed for a free stream velocity of $U_\infty = 40\,m/s\,(Re_{1/7} = 3.6 \times 10^5)$ with an angle of attack of $\alpha = -2°$ and a sideslip angle of $\beta = 0°$. In the wind tunnel campaign, surface pressure measurements have been conducted. Further details on the pressure measurement techniques can be found in [11].

In Fig. 8, the time-averaged pressure coefficient distribution on the lower side (a), as well as on the upper side (b) in the symmetry plane ($y/l_{ref} = 0$) of the fuselage is presented. A good agreement has been found both on the lower and the upper side. On the lower symmetry line (Fig. 8 (a)), a slightly higher pressure is predicted at a monitor point located on the lower backside of the fuselage. In this region, a recirculation zone (separation bubble) is predicted by the simulation as indicated in Fig. 9. The numerical sim-
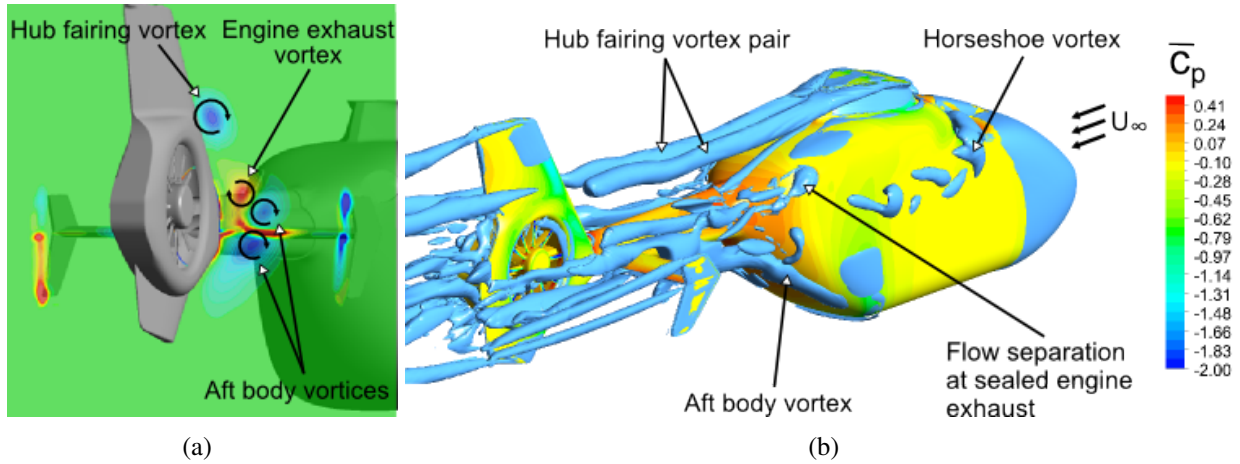
Fig. 10 (a) Instantaneous axial vorticity magnitude at the fan inlet and (b) instantaneous vortical structures visualized by iso-surface of Q-criterion, $Q = 6000\,1/s^2$ for $U_\infty = 62.5\,m/s$, $\alpha = -2°$ and $\beta = 0°$.

ulation underpredicts such a high flow gradient area. In Fig. 8 (c), the flow pattern on the fuselage aft body is visualized by time-averaged surface streamlines. In addition, the time-averaged pressure coefficient distribution in the horizontal plane ($z/l_{ref} = 0.244$) at the fuselage aft body is presented. A good agreement has also been found in this cross-section, except for the region of flow singularity, where the flow on the fuselage separates significantly and slightly higher pressures have been predicted by the numerical simulation.

2.3 CFD Unsteady Results

In this part, the results from the URANS simulation are described. In the present study, on the one hand it is assumed that the main rotor does not significantly influence the Fenestron® flow field characteristics associated with the forward flight condition regarded here and, on the other hand, this kind of flight condition is significant with respect to the Fenestron® noise. Thus, the main rotor is not included in the computational domain and the downwash effect generated by the main rotor is also not taken into account.

2.3.1 Overall Flow Topology

A complex flow topology around the helicopter configuration is predicted by the URANS simulation. In Fig. 10 (b), the instantaneous vorti-

cal structures are represented by an iso-surface of Q-criterion. The time-averaged pressure coefficient distribution is also presented on the fuselage. In the region of the fuselage aft body characterized by a strong curvature, where the pressure rises due to the curved shape, an adverse pressure gradient causes flow separation thereby generating a Counter rotating Vortex Pair (CVP). It trails downstream along the tailboom and interacts with the empennage. Consequently, this CVP is convected downstream to the fan leading to additional pressure fluctuations and possibly impacting on the fan noise. Additional vortical structures are created at the sealed engine exhausts. They interact with the aft body wake and have a slight effect on the flow condition in the vicinity of the fan (Fig. 10 (a)). Further flow separation occurs on the sharp edge of the hub fairing on the upper part of the fuselage thereby generating an additional CVP which is continuously transported downstream to the Fenestron® fin by the main flow. This vortex pair does not directly affect the flow condition at the fan. As previously stated, the engine inlets are also closed. Hence, a relatively large stagnation area is provoked, which induces a horseshoe vortex. They are also convected by the incoming flow along the fuselage side walls and merge downstream with the aft body wake.
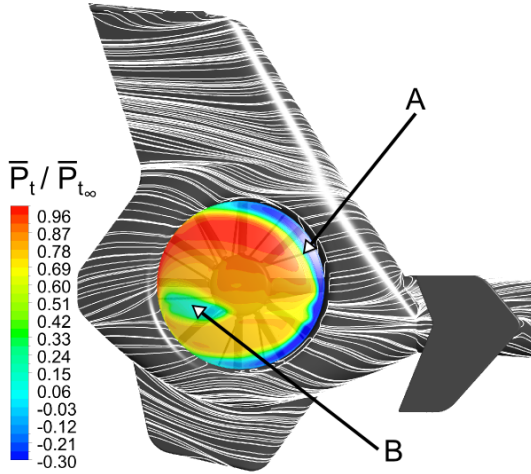
Fig. 11 Time-averaged total pressure distribution at the fan inlet.

2.3.2 Inlet Distortion

Besides vortical structures arising from the fuselage, flow separation occurs at the inlet geometry and leads to a highly non-uniform inflow at the rotor. In Fig. 11, the distribution of time-averaged total pressure ratio is shown at the interface between the ROTOR and the DOMAIN. Note that the rotational direction of the fan is counter-clockwise. The separation bubble caused by boundary layer separation on the inlet lip radius is revealed by a low level of the total pressure ratio (indicated by A in Fig. 11). In addition, a recirculation area is generated behind the advancing side of the rotor hub (indicated by B in Fig. 11). Highly distorted and unsteady blade loading is expected, when the blade is passing through these high turbulent flow regions. This interaction can produce adverse effects on both the fan efficiency and the noise generation.

A detailed investigation of the inlet distortion has been performed based on the power spectral density (PSD) of the pressure fluctuations. An array of monitor points located above the rotor and close to the shroud are considered (Fig. 12 (a)). These monitor points are distributed with an equivalent azimuth angle of 12°. Static pressure values are collected at these points during the 10 fan revolutions for each numerical time step. Fig. 12 (b) shows the result of the PSD analysis as a 2D waterfall plot. Dominant frequen-
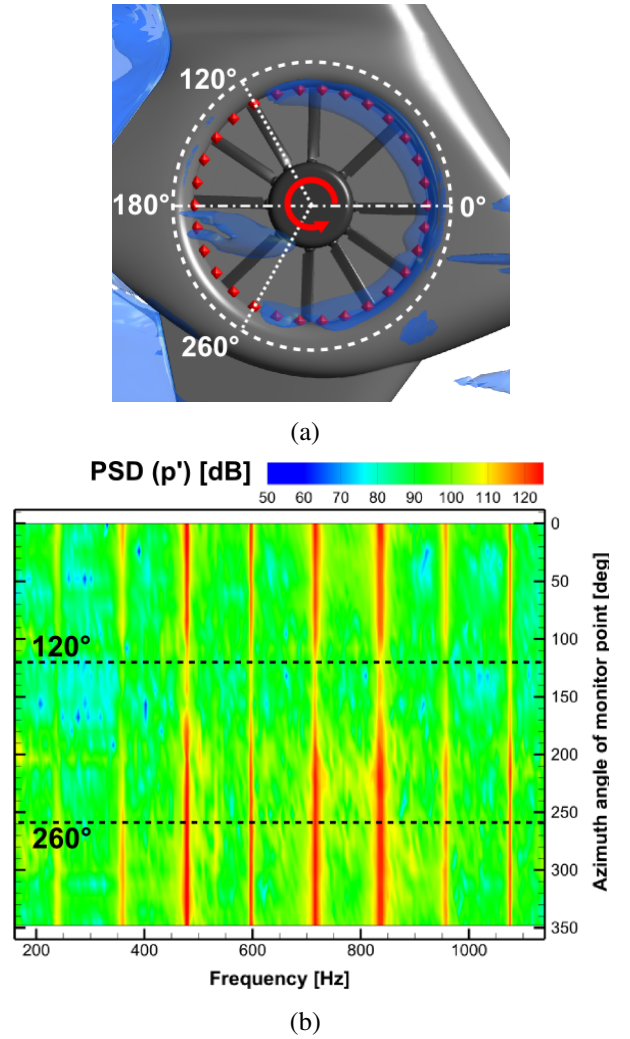

(a)

(b)

Fig. 12 Power spectral density (PSD) analysis of the inlet distorsion.

cies related to the blade passing frequency (BPF) and its sidebands (f_{SB} = BPF±ν) are observed. It can be seen that the interaction between the rotating blades and the separation bubble originating from the inlet lip causes an increase of the pressure fluctuation at the BPF and its sideband frequencies. This statement is confirmed by comparing the dominant peaks at the azimuth angle of θ = 150°, where the inflow is relatively undistorted, to monitor points in the distorted inflow region (0° to 120° and 260° to 360°). The increase of PSD magnitude for 180° to 260° is caused by the interaction of the rotor with separated flow from the hub.
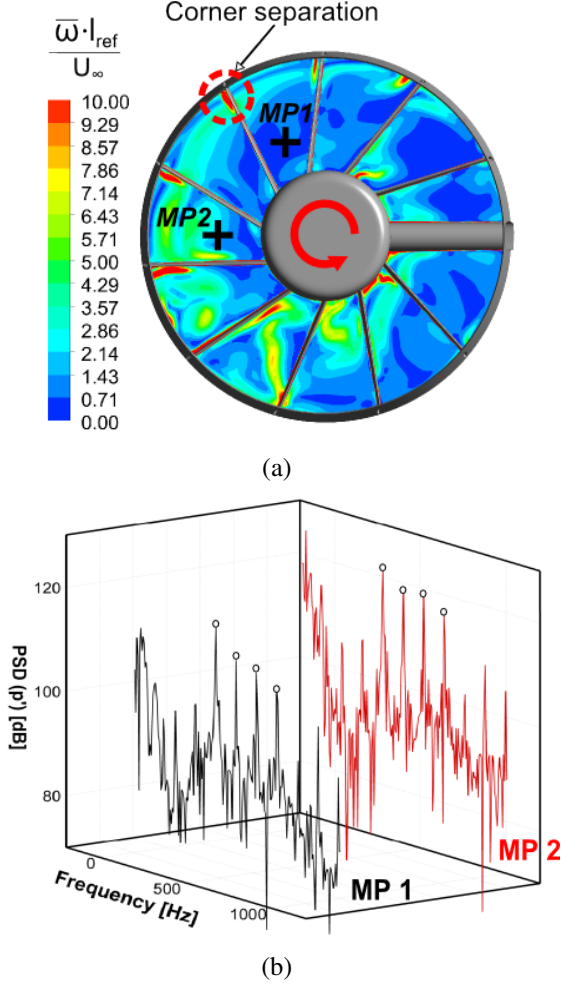
(a)

(b)

Fig. 13 Stator stage flow distortion: (a) distribution of time-averaged vorticity magnitude in the stator stage, (b) PSD analysis at MP 1 and MP 2.

2.3.3   *Stator Row Flow Distortion*

In Fig. 13 (a), a distribution of time-averaged vorticity magnitude is shown for a cross-flow plane located in the stator. The vortical structures generated on the advancing side of the rotor hub and on the inlet lip are transmitted through the rotor passage and consequently provoke a highly fluctuating flow field in the stator row. For the PSD analysis, two monitor points are considered: in the aera of relatively low turbulence (MP 1) and in the highly turbulent region of the stator stage (MP 2). For both monitor points, the BPF and its sideband frequencies are the dominant frequencies (Fig. 13 (b)). However, considerably higher pressure fluctuations are captured at MP 2. At the corner between stator duct and the stator

vane, recirculation areas are also present (corner separation).

3   Computational Acoustic Calculations

Based on the unsteady flow data obtained from the URANS simulation with the SST turbulence model, aeroacoustic calculations have been carried out. In the following section, the employed aeroacoustic formulation and computational setup are briefly presented. Furthermore, the influence of the integration surface location is discussed. Finally, results of the acoustic calculations are reported.

3.1   Computational method

The acoustic code used in the present study was developed at the Universität Erlangen-Nürnberg [12, 13]. The formulation adopted in the code evaluates the acoustic pressure p' in the far-field by solving the integral formulation of the Ffowcs Williams and Hawkings equation [14] on a control surface. The transient data obtained from the CFD simulation are interpolated onto the control surface. Hereby, the control surface has been designed to contain all significant flow non-linearities generating sound. The interpolated data are thus regarded as a new noise source.

In the present study, an integral formulation of the FW-H equation modified by Farassat (Formulation I of Farassat) is applied, which has been used for helicopter rotor and propeller noise prediction [15, 16]. According to this formulation, the predicted sound pressure p' can be decomposed as [17]:

$$p'(\vec{x},t) = p'_T(\vec{x},t) + p'_L(\vec{x},t) + p'_Q(\vec{x},t) \qquad (7)$$

where p'_T is thickness noise and p'_L loading noise, also known as monopole and dipole sources, respectively. Both terms can be rearranged in intergral forms by introducing new variables U_i and L_i defined by Francescantonio [18]:

$$U_i = \frac{\rho}{\rho_0} u_i \qquad (8)$$

$$L_i = P_{ij} n_j + \rho u_i u_n \qquad (9)$$

with u_i the local flow velocity, n_i normal vector pointing away from the control surface, P_{ij} the compressible stress tensor and r_i the position vector from the surface source to the observer position. The integral forms of p'_T and p'_L for a porous, stationary surface can then be written as:

$$4\pi p'_T(\vec{x},t) = \frac{\partial}{\partial t} \int_s \left[\frac{\rho_0 U_n}{R} \right]_{adv} dS \qquad (10)$$

$$4\pi p'_L(\vec{x},t) = \frac{1}{c_0} \frac{\partial}{\partial t} \int_s \left[\frac{L_r}{R} \right]_{adv} dS + \int_s \left[\frac{L_r}{R} \right]_{adv} dS \qquad (11)$$

with ρ_0 the density, c_0 the speed of sound and R the distance between the control surface and the oberver position. Hereby, the subscript n and r refers to the normal component and the radial component of the vector, respectively. The other subscript *adv* denotes that the integration is conducted using the advanced time approach presented by Casalino [19] and defined as:

$$\tau_{adv} = t + \frac{R}{c_0} \qquad (12)$$

where t is the emission time at which the FW-H caculation is performed on the control surface. The term p'_Q in Eq. (7) is the quadrupole noise. Here, the strength of the quadrupole source is generally very small. Thus, the quadrupole term in Eq. (7) is neglected in the present study.

3.1.1   Setup of Acoustic Simulation

The transient quantities including static pressure $p(\vec{x},t)$, density $\rho(\vec{x},t)$ and all three components of the velocity vector $\vec{U}(\vec{x},t)$ have been stored every three numerical time steps ($\Delta t_{CAA} = 3 \times \Delta t_{CFD}$) over the last 10 fan revolutions corresponding to a physical time of $16.92\,ms$. Overall, 1200 samples are taken from the URANS simulation. The frequency resolution of the sound spectrum corresponds to approximately $6\,Hz$.

In order to perform the FW-H surface integral calculation, the obtained instantaneous flow data have been interpolated on a control surface for all acoustic time steps by using in-house written CFD macros. For the integral surface method
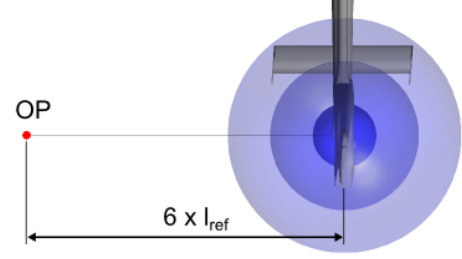
(a)
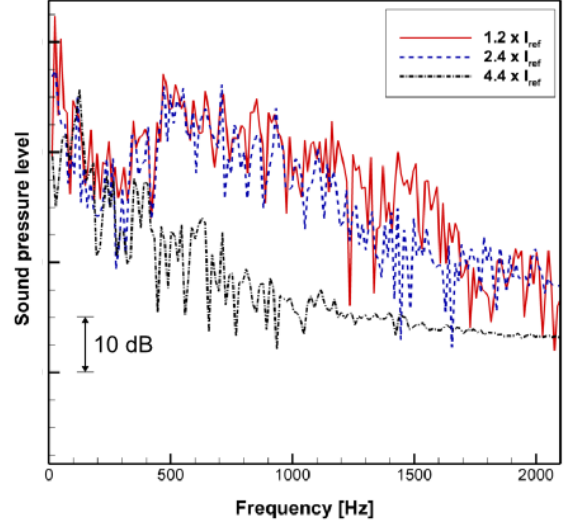
(b)

Fig. 14   Influence of the integral surface location: (a) integral surfaces with three different diameters ($1.2 \times l_{ref}$, $2.4 \times l_{ref}$ and $4.4 \times l_{ref}$), (b) calculated sound pressure levels for an observer point (OP) with distance of $6 \times l_{ref}$.

such as the FW-H formulation and the Kirchhoff's formulation [20], it is recommended that the control surface should include all flow non-linearities in the Fenestron® region producing noise. Thus, the influence of the integration surface diameter has been investigated by considering three spherical control surfaces (centered on the Fenestron®, Fig. 14 (a)). The comparison of the predicted sound pressure level (SPL) at the observer point (OP) shows that the increase of the control surface diameter leads to the decrease of SPL (Fig. 14 (b)). Although the largest control surface can envelope most flow non-linearities, the surface $1.2 \times l_{ref}$ is preferred to reduce the effect of numerical dissipation of the CFD (coarser CFD mesh with increasing dis-

tance to the Fenestron®). This integration surface consists of two disconnected hemispherical parts which are slightly larger than the fan diameter. They are positioned on the fan inlet and outlet to envelop all flow non-linearities caused by the inlet distortion. These control surfaces have been meshed with ICEM CFD and resolved by quadrangular elements with a ratio of 1 : 1 between CFD grid and acoustic grid. The FW-H calculation have been carried out for the various observer points.

The predictive capability of the hybrid approach employed in this study has been assessed for a generic fan-in-wing configuration (consisting of a wing embedded lift-fan) by comparison to acoustic measurements in a related work [21]. The flow phenomenology of this configuration bears strong similarities with the Fenestron® (e.g.: ducted fan flow, inlet distortion). The aerodynamic characteristics of this generic fan-in-wing configuration have been extensively studied in previous research [22, 23]. Following this work, acoustic calculations has been done. In this case, an identical hybrid approach (URANS with ANSYS CFX solver combined with an in-house acoustic code based on the FW-H analogy) is employed to compute the sound pressure levels in the far-field. The predicted sound pressure levels of this configuration are compared to experimental data gathered in the acoustic wind tunnel of BMW in Munich, Germany. For the first and second harmonics, a good agreement has been found in terms of sound pressure level and frequency distribution for all observer points investigated [21].

3.2 Acoustic Results

In this section, results of the FW-H calculations are presented and a qualitative comparison is made with an analytical solution. Note that in the present study the broadband noise has not been evaluated. Furthermore, the acoustic interference effects, such as reflection, scattering and diffraction caused by the duct and blades are not taken into account.
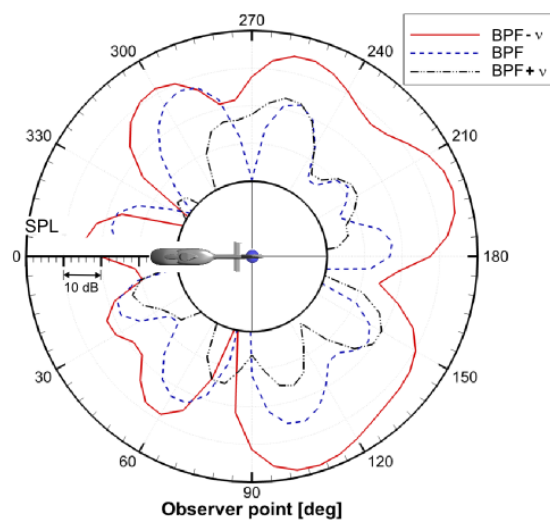
The sound pressure time series calculated for an
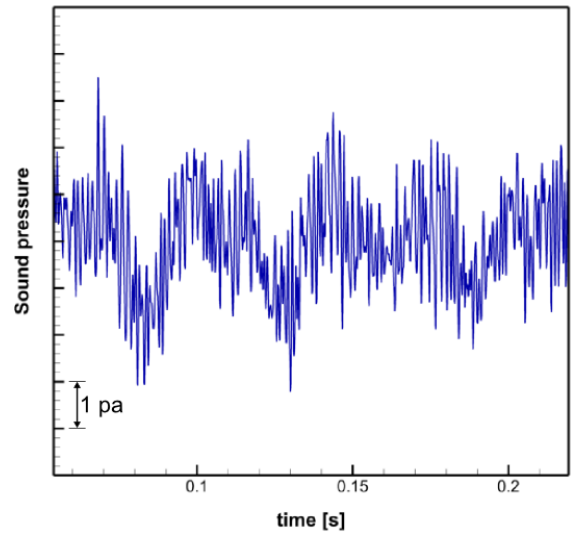
(a)
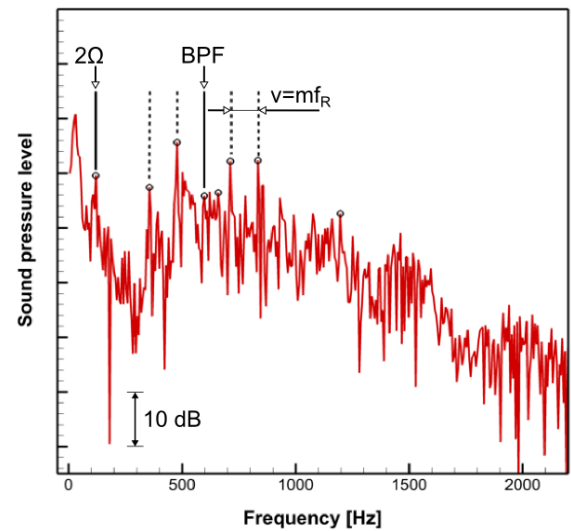
(b)

(c)

Fig. 15 Results of the FW-H caculation: (a) sound pressure, (b) sound pressure level and (c) directivity for the observer point with distance of $18 \times l_{ref}$.

11

observer point located at the fan outlet side on the fan rotational axis with a distance of $18 \times l_{ref}$ is shown in Fig. 15 (a). The corresponding sound pressure level spectrum is presented in Fig. 15 (b). As expected, the energy of the BPF tone (dominant for an evenly spaced rotor), speads out to the neighbor frequency bands (sideband frequencies). A good agreement with the analytical solution of the Fenestron® blades phase modulation is found for the frequencies of the related spectral peaks (BPF and sidebands, see Sec. 1.1). The asymmetrical tone magnitude of the sidebands to the BPF tone is also well predicted by the simulation. Thus, the low frequency sideband ($f_{SB} = 1^{st}$BPF-ν) results in the maximum of the sound pressure level. Since the rotor is designed $180°$ symmetrically in the circumferential direction, the peak at the frequency of $2 \times \Omega$ also appears as dominant.

In Fig. 15 (c), directivities of the calculated sound pressure level are plotted for three dominant frequencies (1^{st}BPF, 1^{st}BPF-ν and 1^{st}BPF+ν , respectively). It can be seen that the predicted tonal noise is more intense downstream than upstream. Considerably high sound pressure level at the fan inlet side at the azimuth angle range between $275°$ to $280°$ might be caused by the inlet distortion.

4   Conclusion and Outlook

Aeroacoustic investigations were conducted on a helicopter fuselage-tail configuration with ducted tail rotor by means of a hybrid approach. Unsteady flow data were obtained from URANS simulation results and served as input to a Ffowcs Williams and Hawkings analogy. The detailed Fenestron® geometry was modeled and the fan rotation was simulated using a sliding mesh approach. The predictive capability of the CFD approach has been assessed by comparison to experimental data of a wind tunnel model with closed Fenestron®. A detailed analysis of the flow around the Fenestron® has been conducted. In cruise, the fan operates under severe conditions. Flow separations on the inlet lip causes a significant distortion giving rise to the noise

level. Results of the acoustic simulation show a good agreement in terms of sideband frequency prediction. The sound directivity in cruise has been reported.

Further work will be performed to correlate the noise sources with the far-field sound pressure levels applying SAS (Scale Adaptive Simulation). The effect of the cross-flow on the Fenestron® noise emission will be assessed by comparison with a helicopter simulation in hover.

Acknowledgments

References

[1] Vuillet, A. and Morelli, F., *New Aerodynamic Design of the Fenestron for Improved Performance*, 20th European Rotorcraft Forum, Garmisch-Partenkirchen, Germany, Sept. 22-25, 1986.

[2] Niesl, G. and Arnaud, G., *Low Noise Design of The EC 135 Helicopter*, American Helicopter Society, 52nd Annual Forum, Washington, D.C., United States, June 4-6, pp. 32-44, 1996.

[3] Alpman, E., Long, L. N. and Kothmann, B. D., *Toward a Better Understanding of the Ducted Rotor Antitorque and Directional Control in Forward Flight*, American Helicopter Society, 59th Annual Forum, Phoenix, AZ, May 2003.

[4] Mouterde, E., Sudre, L., Dequin, A. M., D'Alascio A. and Haldenwang, P., *Aerodynamic Computation of Isolated Fenestron in Hover Conditions*, 33rd European Rotorcraft Forum, Kazan, Russia, Sept. 11-13, 2007.

[5] D'Alascio, A., Le Chuiton F., Mouterde, E., Sudre, L., Kirstein, S. and Kau, H.-P., *Aerodynamic study of the EC135 Fenestron in Hovering*

Flight Conditions by Means of CFD, American Helicopter Society 64th Annual Forum, Montréal, Canada, Apr. 29 - Mai 1, 2008.

[6] Roger, M. and Fournier, F., *An Analysis of In-Fan Tail Rotor Noise*, 20th European Rotorcraft Forum, Garmisch-Partenkirchen, Germany, Sept. 22-25, 1986.

[7] Weisgerber, M. and Neuwerth, G., *Influence of a Helicopter Tail Rotor Shroud on the Interaction Noise due to the Main Rotor Vortices*, 29th European Rotorcraft Forum, Friedrichshafen, Germany, Sept. 16-18, 2003.

[8] Ewald, D., Pavlovic, A., and Bollinger, J. G., *Noise Reduction by Applying Modulation Principles*, Journal of Acoustical Society of America, Vol. 49, Issue 5A, pp. 1381-1385, 1971.

[9] ANSYS, Inc., *CFX-Solver Theory Guide Release 13.0*, Nov. 2010.

[10] Menter, F. R., *Two-Equation Eddy-Viscosity Turbulence Models for Engineering Applications* AIAA Journal, Vol. 32, No. 8, pp. 1598-1605, 1994.

[11] Vogel, F., Breitsamter, C. and Adams, N. A., *Aerodynamic Investigations on a Helicopter Fuselage*, 29th AIAA Applied Aerodynamics Conference, Honolulu, Hawaii, Jun. 27-30, 2011.

[12] Scheit, C. L., *Implementation of Ffowcs Williams and Hawkings (FW-H) Method for Aeroacoustic Prediction*, Master Thesis, Universität Erlangen, 2008.

[13] Scheit, C. L., Karic, B. and Becker, S., *Effect of Blade Wrap Angle on Efficiency and Noise of Small Radial Fan Impellers - A Computational and Experimental Study*, Journal of Sound and Vibration, Vol. 331, No. 5, pp. 996-1010, 2012.

[14] Ffwocs Williams, H., *Sound Generation by Turbulence and Surfaces in Arbitrarary Motion*, Philosophical Transactions of the Royal Society of London, Ser. A, A264, pp. 321-342, 1969.

[15] Farassat, F., *Linear Acoustic Formulas for Calculation of Rotating Blade Noise*, AIAA Journal, Vol. 19, No. 9, pp. 1122-1130, 1981.

[16] Farassat, F., *Derivation of Formulations 1 and 1A of Farassat*, NASA Technical Memorandum, NASA/TM-2007-214853, 2007.

[17] Lyrintzis, A. S., *Surface Integral Methods in Computational Aeroacoustics - From (CFD) Near-Field to the (Acoustic) Far-Field*, Interna-tional Journal of Aeroacoustics, Vol. 2, No. 2, pp. 95-128, 2003.

[18] Di Francescantonio, P., *A New Boundary Integral Formulation for The Prediction of Sound Radiation*, Journal of Sound and Vibration, Vol. 22, No. 4, pp. 491-509, 1997.

[19] Casalino, D., *An Advanced Time Approach for Acoustic Analogy Predictions*, Journal of Sound and Vibration, Vol. 261, No. 4, pp. 583-612, 2003.

[20] Kirchhoff, G. R., *Zur Theorie der Lichtstrahlen*, Annalen der Physik und Chemie, Vol. 254, Issue 4, pp. 663-695, 1883 .

[21] Tirakala, J., Thouault, N., Breitsamter, C., and Adams, N. A., *Aeroacoustic Investigations of a Generic Fan-in-Wing Configuration*, Internoise, Osaka, Japan, Sept. 4-11, 2011.

[22] Thouault, N., Breitsamter, C., and Adams, N. A., *Numerical Investigation of Inlet Distortion on a Wing-Embedded Lift Fan*, AIAA Journal of Propulsion and Power, Vol. 27, No. 1, pp. 16-28, 2011.

[23] Thouault, N., *Aerodynamic Investigation on Generic Fan-in-Wing Configurations*. PhD Thesis, Technische Universität München, Germany, 2010.

Copyright Statement